Effect of Molecular Elasticity on Out-of-Plane Orientations in Shearing Flows of Liquid-Crystalline Polymers

R. G. Larson*,† and H. C. Öttinger‡

AT&T Bell Laboratories, Murray Hill, New Jersey 07016, and Institut für Polymere, Eidgenössische Technische Hochschule Zürich, ETH-Zentrum, CH-8092 Zürich, Switzerland

Received April 26, 1991; Revised Manuscript Received June 21, 1991

ABSTRACT: The Doi equation for the time-dependent orientational distribution function of rodlike molecules in a nematic monodomain is solved for startup of a simple shearing flow with director orientation initially oriented at various angles with respect to the shearing plane, where the shearing plane is defined to be parallel to both the velocity and its gradient. Two numerical solution techniques are used; one is an expansion in spherical harmonic functions, which is a generalization of a technique derived earlier for a director confined to the shearing plane, and the second is a stochastic method that integrates the equations of motion for a large ensemble of molecules. We find that at low and modest shear rates, the director can be attracted either to a time-periodic tumbling orbit that lies in the shearing plane or to an orbit that lies out of the shearing plane. This latter orbit is either a steady "log-rolling" state with average orientation perpendicular to the shearing plane or a time-periodic "kayaking" state with an orbit oblique to the shearing plane. The final state of the system depends on the shear rate and the strength of the nematic potential. In some cases both the in-plane tumbling and log-rolling (or kayaking) states are attractors; the final state then depends on the initial director.

I. Introduction

Recent experimental studies on shearing flows of lyotropic liquid-crystalline polymers (LCP's) have shown that director tumbling can occur at low shear rates in specimens that are untextured—that is, specimens that are free of orientational inhomogeneities.[1,2] The director in a nematic material is the direction of average molecular orientation, where the average is taken spatially over a region large enough to contain many molecules. Tumbling is here defined to be the time-periodic rotation of the director in a shearing flow. Tumbling has also been both predicted and shown experimentally to occur in some small-molecule nematics when the temperature is close to that for a transition to a smectic-A phase.[3,4]

In polymeric nematics, tumbling was predicted in 1983 by Semenov[5] and in 1984 by Kuzuu and Doi[6] using Doi's molecular theory of untextured polymeric nematics;[7] but this prediction was treated with skepticism until recent theoretical work and the experimental work mentioned above. Marrucci and Maffetone[8] showed theoretically that the tumbling predicted by Doi and Kuzuu can be suppressed at high rates of shear and that suppression of tumbling has important consequences for the rheological properties of LCP's in shearing flows. In particular, they showed, using a simplified two-dimensional version of the Doi model for nematic LCP's, that the cessation of tumbling is associated with a negative first normal stress difference N_1. In a full three-dimensional time-dependent solution of the Doi equation, Larson[9] confirmed the results of Marrucci and Maffetone and described in some detail how the molecular dynamics undergo two transitions as the shear rate is increased. The first is a transition from tumbling to "wagging"—i.e., a oscillation of the direction of average molecular orientation between two limiting angles. The second is a transition from wagging to a steady-state direction of average molecular orientation. Both transitions are also found in the two-dimensional calculations;[8] each transition is associated with a predicted change in sign of the time-averaged value of N_1. As the shear rate increases, the time-averaged value of N_1 is predicted to change from positive to negative, and then back to positive. The predicted transitions in the first normal stress difference have been observed in lyotropic polymeric nematics and cholesterics[10–12] and to some extent in thermotropics.[13,14] In addition, the predicted shear-rate dependences of the time-averaged first and second normal stress differences are in good qualitative agreement with recent measurements,[15] thus lending added credibility to the validity of Doi's molecular theory. The transitions in molecular dynamics and the sign changes in N_1 are qualitatively similar in two vis-à-vis three dimensions and are also insensitive to the particular form of the potential used to simulate nematic interactions among molecules.[8,9]

Although this qualitative agreement between theory and experiment is encouraging, there are ambiguities in the interpretation of the theory and in its application to the experimental systems. While the predictions for the regime of steady-sate orientation at high shear rates can be compared directly to the corresponding experimental measurements, the predictions are problematic at lower shear rates where tumbling and wagging are predicted and the stresses for an untextured specimen are predicted to oscillate in time. The samples studied rheologically were textured at rest—that is, they contained many orientational defects and inhomogeneities. If the theory is accurate in its prediction that at high shear rates a steady-state average orientation should exist, then these inhomogeneities should diminish after prolonged shearing at high rates and be of little consequences to the steady-sate rheology. However, at low shear rates in the tumbling regime, there is no steady-state orientation, and it seems unlikely that even prolonged shearing could produce uniformity in orientation. Indeed, visual observations suggest that, at low shear rates, gradients in orientation increase when shearing starts.[16,17] In the work referred to

† AT&T Bell Laboratories.
‡ Eidgenössische Technische Hochschule Zürich.

0024-9297/91/2224-6270$02.50/0

above,[8,9] the Doi theory for an untextured specimen was therefore made to apply to the textured experimental systems by assuming that the net stress measured on a bulk textured sample is the time average of the stress for an untextured sample. In the tumbling regime, this time average was taken over a period of the tumbling motion, with the director tumbling *in the shearing plane*.

In textured samples, however, the director is not initially in the shearing plane, and even if it were, if would not necessarily remain there under a shearing flow. Recent calculations show that in the tumbling regime *director gradients* can create flow instabilities that drive the director out of the shearing plane.[18] Director gradients are produced even when the sample starts out as a uniform monodomain with the director in the shearing plane, because the molecular orientation is ordinarily pinned at the walls of the shearing device and during shearing tumbling in the bulk of a sample leads to a spatial "winding up" of the director and thereby to an increasing gradient in orientation.[19,20] (The spatial winding up that can exist at steady-sate is typically called "tumbling" in the literature on small-molecule nematics. Here, however, we use the term to refer to periodicity in time rather than space.) Instabilities to out-of-plane director orientations have indeed been found in shearing flows of the small-molecule nematic *p*-cyanobenzylidene-*p'*-octylaniline (CBOOA) in a temperature range where tumbling is expected.[3]

While director gradients, which can produce an out-of-plane component of the director orientation, are present in both small-molecule and polymeric nematics, at easily accessible shear rates only polymeric nematics possess a *molecular* elasticity associated with flow-induced distortions of the degree of molecular alignment or order parameter. The influence of molecular elasticity is quantified by the *Deborah number*, $De \equiv \dot{\gamma}\tau$, where τ is the molecule's rotational relaxation time. Negative values of the first normal stress difference are produced by molecular elasticity when De is order unity or greater, and shearing torques are then large enough to reduce the degree of molecular alignment below that of the equilibrium or rest state.[8]

We shall see in what follows that, in the absence of director gradients, *molecular elasticity can by itself cause the director to move toward or away from the shearing plane*. In particular, we show from the Doi theory with the Onsager potential that at high shear rates molecular elasticity drives the orientation *toward* the shearing plane. At intermediate shear rates, *both the shearing plane and the vorticity axis are attractors for the director*, and the final orbit of the director depends on its initial orientation. The vorticity axis is perpendicular to the shearing plane. At low shear rates, there is only a weak drift of the orientation away from its original orbit, and the direction of the drift depends on the strength U of the nematic potential and on the initial director orientation.

We have been using the term "director" loosely. Strictly speaking, the term applies only when the fluid possesses uniaxial symmetry, which is true in a nematic polymer only at equilibrium or under very slow flow. However, even when the flow is strong, the concept of a direction of average molecular orientation remains useful. Except for degenerate cases, the *birefringence axis* is an appropriate generalization of the director concept; it can be defined as the orientation of the major axis of the order parameter or birefringence tensor,[9] $\boldsymbol{S}$, which will be defined shortly. This major axis is precisely the director when the material is uniaxial and except for degenerate cases, remains well-defined when uniaxial symmetry is broken.

In the following, polymeric nematics will be described by the nonlinear Doi theory, which has been discussed at length elsewhere.[7,9] In brief, the Doi theory gives an equation for the evolution of the molecular orientation-distribution function $\psi(\mathbf{u})$[7]

$$\frac{\partial\psi}{\partial t} + \frac{\partial}{\partial \mathbf{u}}\cdot[(\mathbf{u}\cdot\nabla\mathbf{v} - \mathbf{uuu}:\nabla\mathbf{v})\psi] - \frac{\partial}{\partial \mathbf{u}}\cdot\left\{\hat{D}_r(\mathbf{u})\left[\frac{\partial\psi}{\partial \mathbf{u}} + \psi\frac{\partial}{\partial \mathbf{u}}\left(\frac{V_{ev}}{kT}\right)\right]\right\} = 0 \quad (1)$$

where $\psi(\mathbf{u}')$ is the probability that a rodlike molecule has an orientation given by the unit vector $\mathbf{u}'$, $\nabla\mathbf{v}$ is the velocity gradient, and $\hat{D}_r(\mathbf{u})$ is the orientation-dependent rotary diffusivity, given by

$$\hat{D}_r = D_r\left[\frac{4}{\pi}\int \psi(\mathbf{u}') \sin(\mathbf{u}',\mathbf{u})\, du'^2\right]^{-2}$$

Here D_r is the rotary diffusivity in a hypothetical isotropic solution of molecules at the given concentration, and $\sin(\mathbf{u}',\mathbf{u})$ is the positive sine of the angle between the unit vectors $\mathbf{u}'$ and $\mathbf{u}$ describing the orientations of two rods. The integral is over the surface of a unit sphere in orientation space. Also, in eq 1, $\partial/\partial\mathbf{u}$ is the gradient operator on the unit sphere, and V_{ev} is an effective excluded-volume potential; here we take for V_{ev} the Onsager potential[21]

$$V_{ev} = V_0(\mathbf{u}) = 2cdL^2kT\int \psi(\mathbf{u}') \sin(\mathbf{u}',\mathbf{u})\, du'^2 \quad (2)$$

where d is the rod diameter, L is its length, and c is the number of molecules per unit volume. A two-dimensional version of this equation, with the Maier-Saupe potential replacing that of Onsager, has been presented by Marrucci and Maffetone.[8] When eq 1 is solved numerically for the distribution function ψ, one finds the transitions in the shearing plane among tumbling, wagging, and steady-state orientations, described earlier.[8,9]

Unlike these in-plane transitions, the out-of-plane orientational transitions we describe below are subtle, and small inaccuracies in the solution of the Doi equation can lead to qualitative changes. Thus here we use two highly accurate numerical techniques to solve the Doi equation. The first is an expansion in spherical harmonic functions that extends the method described in refs 9 and 22. The extension presented here allows the director to lie outside the shearing plane. The earlier technique, like the one described here, was three-dimensional in the sense that the molecular orientation distribution function depended on the two Euler angles in three-dimensional space. The symmetry assumed in the earlier calculations confined the director to the shearing plane; the technique was in that sense two-dimensional. Here, this symmetry requirement is lifted so that the technique presented here is three-dimensional in every sense. The details of the spherical-harmonic numerical technique are presented in Appendix A.

The only significant mathematical or numerical approximation in the spherical-harmonic expansion is that the orientation-dependent rotary diffusivity $\hat{D}_r(\mathbf{u})$ is replaced by its average $\overline{D}_r$ over the instantaneous molecular orientation distribution. Thus, within this approximation, all molecules at each instant share a common rotary diffusivity $\overline{D}_r$, but $\overline{D}_r$ still varies in time as $\psi(t)$ is distorted by the flow. To check the qualitative accuracy of this approximation, we use in select cases a second, computationally more expensive, technique to confirm the main conclusions drawn from the results of the spherical-

harmonic technique. In this second method, the orientational histories of a large ensemble of (some 10 000) molecules are calculated by integrating the equations of motion for each molecule. The equation of motion for each molecule contains a convective term to describe the orienting effect of shear flow, a stochastic term to describe Brownian motion, and an excluded-volume interaction term to describe the influence on a given molecule of all the other molecules in the ensemble. These same terms appear in eq 1, which is the equation solved by the spherical-harmonic method, but in the stochastic method $\hat{D}_r(\mathbf{u})$ need not be averaged; it can vary with the orientation $\mathbf{u}$ from rod to rod in the ensemble. The details of the stochastic technique are presented in Appendix B.

II. Results

A. In the Absence of Molecular Elasticity. We first review the known results obtained when molecular elasticity is absent.

In a homogeneous bulk of liquid-crystalline material, well away from director gradients induced for example by bounding surfaces and at shear rates low enough that molecular elastic effects are negligible, the director $\mathbf{n}$ obeys the following evolution equation:

$$\dot{\mathbf{n}} = \mathbf{n}\cdot\omega + \lambda\mathbf{nnn}:\mathbf{D} \tag{3}$$

Here, $\mathbf{n}$, the director, is a unit vector parallel to the direction of average molecular orientation. In a shearing flow, we let x be the flow direction, z the velocity-gradient direction, and y the vorticity direction. Then we have

$$\omega \equiv \frac{\dot{\gamma}}{2}\begin{pmatrix} 0 & 0 & -1 \\ 0 & 0 & 0 \\ 1 & 0 & 0 \end{pmatrix} \tag{4}$$

$$\mathbf{D} \equiv \frac{\dot{\gamma}}{2}\begin{pmatrix} 0 & 0 & 1 \\ 0 & 0 & 0 \\ 1 & 0 & 0 \end{pmatrix} \tag{5}$$

where $\dot{\gamma}$ is the shear rate and is here taken to be positive in sign. In eq 3, λ is a parameter that controls the dynamics of the director. When $\lambda > 1$, the director has two stable steady-state orientations, the first given by $\mathbf{n} = (n_x, 0, n_z)$, with $n_x = \cos\theta$ and $n_z = \sin\theta$, and the second by $n_x = -\cos\theta$ and $n_z = -\sin\theta$, where $\tan^2\theta = (\lambda - 1)/(\lambda + 1)$. There are also *unstable* steady-state solutions of eq 3 that lie in the shearing (x–z) plane, namely, $n_x = -\cos\theta$ and $n_z = \sin\theta$, and $n_x = \cos\theta$ and $n_z = -\sin\theta$. Since the polarity of the director has no physical significance, the two stable (or unstable) solutions can be thought of as different representations of the same stable (or unstable) physical solution, in which the molecules are aligned at an angle of θ (or $-\theta$) with respect to the flow direction. In addition to these solutions in the shearing plane, there is a pair of unstable solutions to eq 3 that is parallel to the vorticity axis; that is, $\mathbf{n} = (0, \pm 1, 0)$.

When $\lambda < 1$, which occurs in at least some (and perhaps most) polymeric nematics, as well as in small-molecule nematics near a transition to a smectic-A phase,[3,4] there are no steady-state solutions, stable or unstable, in the shearing plane. If the director is initially in the shearing plane, then according to eq 3 it *tumbles* continuously in that plane. The period P for rotation through an angle of 2π is given by

$$P = 4\pi/\dot{\gamma}(1 - \lambda^2)^{1/2} \tag{6}$$

If the director starts with an orientation outside the shearing plane, it still tumbles in an orbit with period P, but this orbit is cocked with respect to the shearing plane and has no tendency to drift either toward or away from the shearing plane. When $\mathbf{n}$ is parallel to the vorticity axis, $\mathbf{n} = (0, \pm 1, 0)$, the orbit is degenerate and the angular displacement traversed is zero; this case is therefore the only steady-state solution of eq 3 when $\lambda < 1$. The director, if pushed slightly away from the vorticity axis, merely orbits about the vorticity axis, with no growth or decay of the orbit. Thus the steady-state solution $\mathbf{n} = (0, \pm 1, 0)$ is neutrally stable. By contrast, when $\lambda > 1$, the steady-state solution $\mathbf{n} = (0, \pm 1, 0)$ is unstable; a small displacement from this orientation grows until the director comes to rest in the shearing plane at the stable steady-state flow alignment angle θ.

The marginally stable director orbits for $\lambda < 1$ are identical to the *Jeffreys orbits* traversed by an ellipsoidal particle in a shearing flow;[23] eq 3 applies to an axisymmetric ellipsoid with $\lambda = (r^2 - 1)/(r^2 + 1)$ and $r = L_1/L_2$, where L_1 is the length of the axisymmetry axis of the ellipsoid (which is parallel to $\mathbf{n}$ in eq 3) and L_2 is the length of each of the other two axes.

The marginal stability of every orbit when $\lambda < 1$ holds only when we neglect director gradients and molecular elasticity. We have already noted (in the Introduction) that when the director, held to a fixed orientation at the bounding surfaces, winds up spatially in the shearing plane, director gradients can create instabilities to out-of-plane director motions. It has also been observed experimentally in tumbling small-molecule nematics that the uniform steady-state orientation $\mathbf{n} = (0, \pm 1, 0)$ is stabilized by Frank gradient elasticity when the shear rate is less than a critical value, but above this value "hydrodynamic focusing terms" produce a linear convective instability to rolls aligned parallel to the flow.[24,25] An apparently similar phenomenon has recently been observed in tumbling polymeric nematics; it is recognized optically by the appearance of a "phase grating", i.e., alternating dark and bright stripes.[1,26]

Even when director gradients are absent or neglected, viscoelastic effects can break the marginal stability of the tumbling orbits. According to the recent work of Bruinsma and Safinya,[27] this happens in small-molecule tumbling nematics because of the shear deformation of "cybotactic clusters"—i.e., pretransitional fluctuations with smectic order that form as the transition to a smectic-A phase is approached. The deformation of these fluctuations creates an elastic stress that makes the orbit in the shearing plane unstable and pushes the director toward the vorticity axis.[27] Since in the absence of this viscoelastic effect all orbits are neutrally stable, even at low shear rates—where the viscoelastic effects are small—there is a predicted destabilization of the orbit in the tumbling plane and a stabilization of alignment along the vorticity axis. Because the cybotactic clusters are themselves responsible for the tumbling character of these nematics, when the shear rate is high enough to destroy the clusters, the nematic recovers its aligning character, and the director should tend toward the shearing plane at a stable fixed small angle θ with respect to the flow direction. At intermediate shear rates, stable director orientations are predicted to exist both in the flow-aligned direction in the shearing plane and along the vorticity axis.[27] Below, we predict a similar pattern of stability transitions with increasing shear rate for polymeric nematics in which deformation of the molecular order parameter, rather than of cybotactic clusters, produces the transitions.

B. Effect of Molecular Elasticity. According to eq 2, the strength of the nematic interactions between

molecules is proportional to

$$U \equiv 2cdL^2 \tag{7}$$

For a given molecular length L and diameter d, U is proportional to the polymer concentration c. The value $U = 10.67$ is the lowest for which the theory predicts that a fully liquid-crystalline phase will form that is stable to both orientational and concentration fluctuations. In what follows, we present theoretical results for $U = 10.67$, $U = 12$, and $U = 14$. We also consider various dimensionless shear rates $\Gamma \equiv \dot{\gamma}/D_r$, where D_r is the rotary diffusivity in a hypothetical isotropic solution of molecules at the given value of U. Since the molecular relaxation time τ is inversely proportional to D_r, Γ is proportional to the Deborah number.

In an earlier work,[9] spherical-harmonic solutions of the Doi equation were obtained with ψ initially at equilibrium and with the director initially in the shearing plane, specifically in the z direction—that is, parallel to the gradient in velocity. Here we allow the director to reside initially at some angle ϕ between the z and y axes. Thus, when $\phi = 0°$, the director is parallel to the z axis, and when $\phi = -90°$, it is parallel to the y, or vorticity, axis. In general, the initial director is defined by $(n_x, n_y, n_z) = (0, \sin\phi, \cos\phi)$. Once flow starts, the orientation distribution no longer remains uniaxial and the director is no longer defined. The instantaneous average molecular orientation is then quantified by the order parameter tensor

$$\mathbf{S} \equiv \int \psi(\mathbf{u}) \left[\mathbf{uu} - \frac{1}{3}\delta\right] du^2 \tag{8}$$

where δ is the unit tensor. The scalar order parameter $S \equiv ((3/2)\mathbf{S}:\mathbf{S})^{1/2}$ represents the degree of molecular alignment. In the absence of flow, $S = S^{eq}$, where $S^{eq} = 0$ constitutes an isotropic phase, and $S^{eq} \to 1$ represents perfect alignment, achieved only when $U \to \infty$. Of particular interest to us is the quantity $S_2 \equiv S_{zz} - S_{yy}$. When the average orientation is predominantly parallel to z, S_2 is roughly S^{eq}, when it is parallel to y, S_2 is close to $-S^{eq}$, and when the orientation is on average parallel to x, S_2 is near zero. Thus, by plotting S_2 versus shear strain $\gamma \equiv \dot{\gamma}t$, we can easily distinguish any drift of the molecular orientation either toward or away from the shearing plane or the vorticity axis.

1. Results for $U = 10.67$ with Averaged Rotary Diffusivity. We first solve the Doi equation with averaged rotary diffusivity using the spherical-harmonic technique. In this method, infinite summations are truncated at a finite value l_{max}, of a summation index l; see Appendix A. Here we take $l_{max} = 12$; for this case the distribution function ψ is represented by 90 spherical-harmonic functions. A few refined calculations with $l_{max} = 16$ (152 spherical-harmonic functions) suffice to show that $l_{max} = 12$ gives accurate results for $U = 10.67$ and $U = 12$.

Figure 1 shows S_2 versus γ for $\Gamma = 7$, and with the initial director orientation at angles ϕ of 0°, −24.55°, −45°, −60°, −75°, and −90° with respect to the shearing plane. We note that previous work[9] showed that tumbling occurs for $\Gamma \leq 9.5$ when $U = 10.67$; thus the results for $\Gamma = 7$ depicted in Figure 1 are within the tumbling region. In all cases in Figure 1, except the singular case of $\phi = -90°$, there is a periodic oscillation of S_2 with a period of about 15 strain units; this oscillation reflects the tumbling motion of the birefringence axis.[9] When $\phi = -90°$, the director is initially perpendicular to the shearing plane, and tumbling is not possible; thus S_2 does not oscillate but remains nearly constant at a value of S_2 near $-S^{eq}$. When the initial director angle ϕ is 0°, S_2 oscillates between 0 and roughly $S^{eq} = 0.792$; thus, as the birefringence axis tumbles, it remains in the shearing plane. When ϕ is reduced, there

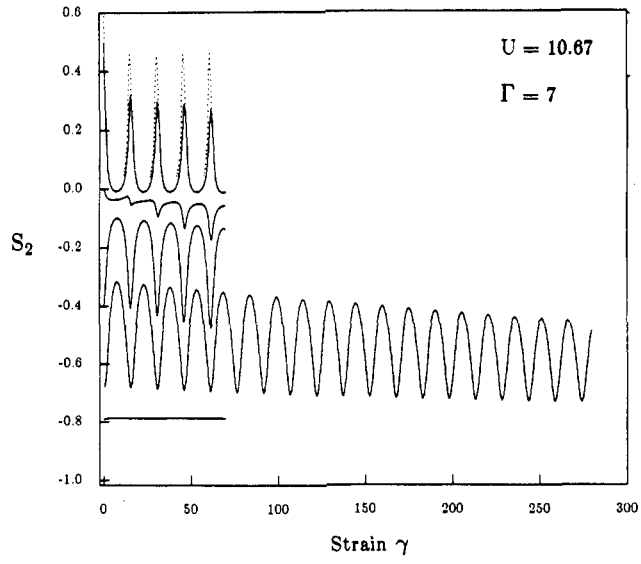

Figure 1. S_2 versus shear strain γ for $\Gamma = 7$ and $U = 10.67$. The initial director angles ϕ, from top to bottom, are 0° (dashed line), −24.55°, −45°, −60°, −75°, and −90°.

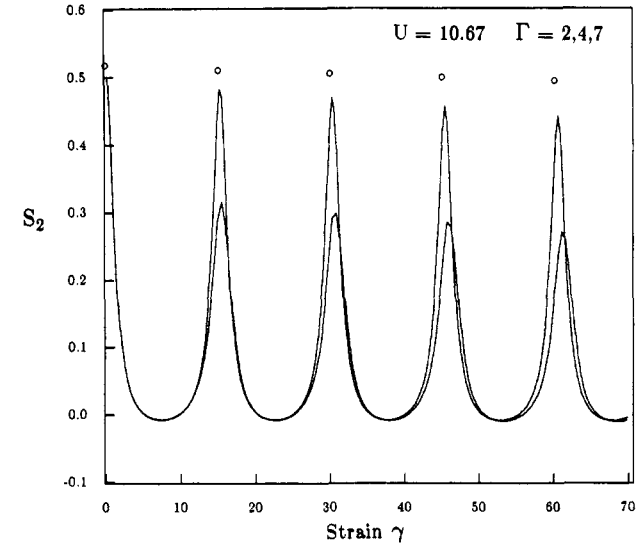

Figure 2. S_2 versus shear strain γ for $\Gamma = 2$ (points), 4 (top line), and 7 (bottom line) with $U = 10.67$. The initial director angle ϕ is −24.55°. For $\Gamma = 2$, only the maxima in S_2 are shown.

is an out-of-plane component of the tensor $\mathbf{S}$; hence, S_2 varies from slightly negative to a value less than S^{eq} as the birefringence axis tumbles. The out-of-plane component grows slowly with time, as the birefringence axis spirals toward the vorticity direction. This approach toward the vorticity axis occurs at all angles investigated; these range from −9.55° to −75°. The approach toward the vorticity axis is slow; from Figure 1 it is clear that, although the run with an initial angle of −75° was continued out to a final strain of 280, many more strain units, perhaps thousands, would be required to bring the birefringence axis parallel to the y direction.

A similar pattern is found for other shear rates Γ less than 7, at least down to the lowest investigated, namely, $\Gamma = 2$. Figure 2 shows S_2 versus strain γ when $\phi = -24.55°$ for $\Gamma = 2$, 4, and 7. At each shear rate, the maximum in S_2 diminishes with each oscillation, although the rate of decrease is lessened as Γ is reduced. In the limit $\Gamma \to 0$, the net rate of drift, averaged over a period of the oscillation, of the birefringence axis toward the vorticity axis, must approach zero, since in that limit molecular-viscoelastic effects disappear, and according to eq 1 all orbits become neutrally stable. *Thus all results for* $\Gamma \leq$

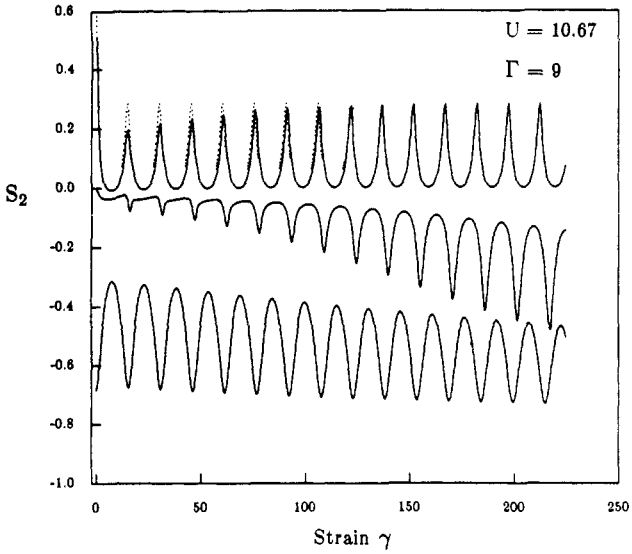

Figure 3. S_2 versus shear strain γ for $\Gamma = 9$ and $U = 10.67$. The initial director angles ϕ, frm top to bottom, are 0° (dashed line), -24.55°, -45°, and -75°.

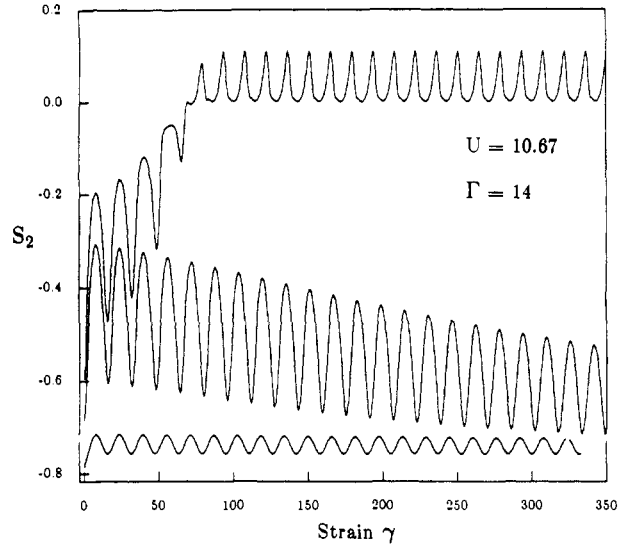

Figure 4. S_2 versus shear strain γ for $\Gamma = 14$ and $U = 10.67$. The initial director angles ϕ, from top to bottom, are -69.55°, -75°, and -86.71°.

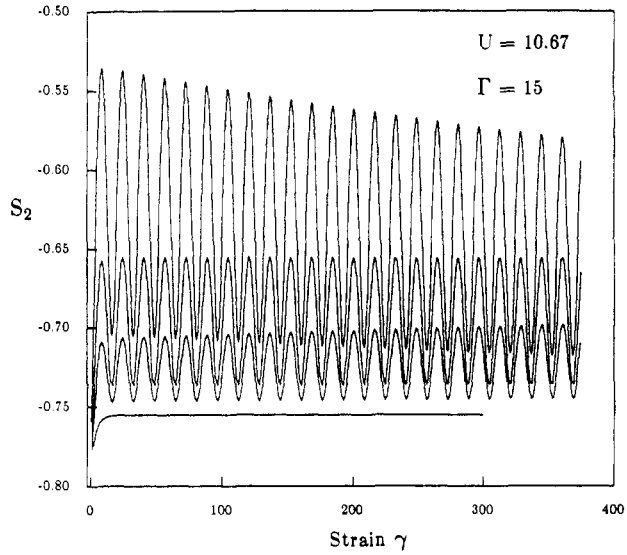

Figure 5. S_2 versus shear strain γ for $\Gamma = 15$ and $U = 10.67$. The initial director angles ϕ, from top to bottom, are -81.95°, -85.09°, -88.35°, and -90°.

7 and $U = 10.67$ are consistent with the conclusion that the vorticity direction is the only stable attractor for the birefringence axis. For initial director angles other than 0°, the birefringence axis drifts toward the vorticity direction; when it reaches the vorticity axis, a steady-state orientation distribution is attained. We call this solution the "log-rolling" state, since we imagine that if the rods had a finite diameter, they would roll in the shearing flow like logs on a river.

When Γ is increased to 9, which is still (just barely) within the tumbling regime, initial director orientations that are close enough to the shearing plane are attracted to the shearing plane, while the majority of orientations are still attracted to the log-rolling state. Figure 3 shows for this case that when $\phi = -24.55°$, the birefringence axis is drawn, within about 100 strain units, to the shearing plane. For the other initial orientations studied, namely, those with $\phi \leq -45°$, the vorticity axis is still the attractor. Note that the final approach to the vorticity axis is very slow, much slower than the approach to the shearing plane when the shearing plane is the attractor. This difference in strength of attraction between the shearing plane and the vorticity axis is a consistent feature of all our simulations.

As Γ is increased further, into the wagging regime where $\Gamma \geq 10$, the range of angles ϕ for which the shearing plane is the attractor increases. Figure 4, for example, shows that when $\Gamma = 14$, angles $\phi \leq -75°$ are attracted to the vorticity axis, while angles $\phi \geq -69.55°$ are all within the domain of attraction to the shearing plane. Once it reaches the shearing plane, the birefringence axis executes a wagging motion at this shear rate.[9] At this value of U, wagging occurs for $10 \leq \Gamma \leq 22$. As Γ is increased yet further, the vorticity axis is finally not an attractor at all. It disappears, however, in a surprising way. Rather than simply shrinking to zero, like the smile of the Cheshire cat, at the last moment before disappearing it moves away from the vorticity direction and assumes some small angle with respect to it. This occurs at Γ between 14 and 15. Figure 5 shows that, for an initial angle of $\phi = -86.71°$ at $\Gamma = 15$, the birefringence axis moves slowly away from the vorticity axis, but, for $\phi = -85.09°$, it oscillates in a nearly fixed orbit. For $\phi = -81.95°$, S_2 drifts (while oscillating) toward lower values, apparently toward the stable orbit obtained for $\phi = -85.09°$. Thus the stable orbit obtained for -85.09° is an *attractor*, since it draws in the birefringence axis from some finite domain of attraction covering angles both above and below the nearly stable angle of -85.09°. When ϕ is exactly -90°, the birefringence axis remains along the vorticity direction, because a finite, though possibly small, disturbance is required to obtain a finite rate of drift toward the stable orbit. The shearing plane is also an attractor for this value of Γ; Figure 6 shows that, for $\phi = -75°$, the birefringence axis moves toward the shearing plane, while for $\phi = -79°$ it moves in the opposite direction, although this very slow drift is hard to detect in Figure 6. Thus, for $\Gamma = 15$, the shearing plane is an attractor, where wagging occurs, and the second stable orbit is an attractor that is close to, but not coincident with, the vorticity axis. This second stable orbit resembles the paddle motion used to propel an eskimo's kayak.

The stable "kayaking" orbit persists over only a very slender range of shear rates, however. It exists for Γ = 14.5 and $\Gamma = 15$, but at $\Gamma = 16$, the shearing plane is the only attractor; see Figure 7. Figure 7 also shows that the rate of approach to the shearing plane accelerates quickly as Γ is increased; when $\Gamma = 17$, the approach is already very rapid.

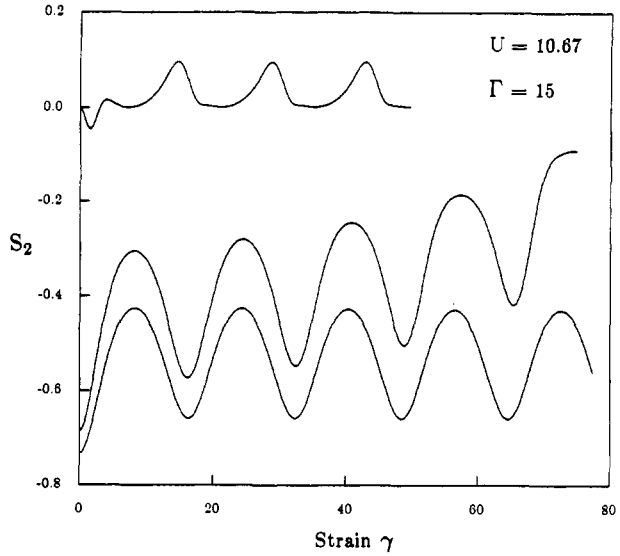

Figure 6. S_2 versus shear strain γ for $\Gamma = 15$ and $U = 10.67$. The initial director angles ϕ, from top to bottom, are −45°, −75°, and −79°.

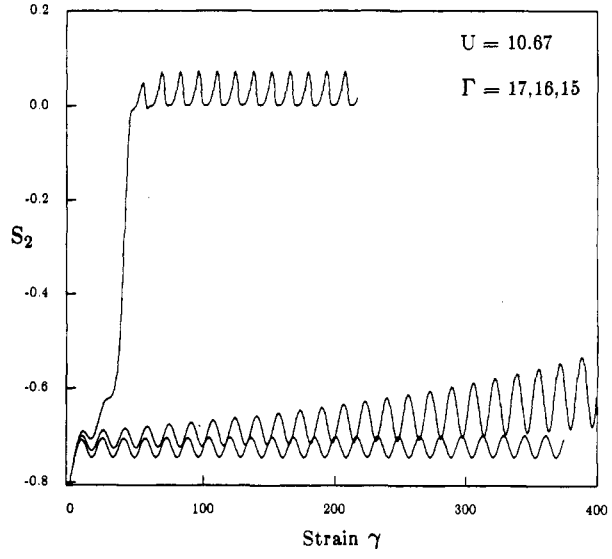

Figure 7. S_2 versus shear strain γ for $U = 10.67$ and an initial director angle ϕ of −86.71°, for Γ, from top to bottom, of 17, 16, and 15.

Figure 8 shows that, for $\Gamma = 18$ and more, shear-induced distortions of **S** become so severe that, even when the initial orientation is exactly −90°, the molecules quickly find their way toward the shearing plane. In these cases, no fluctuations from the log-rolling state are needed to obtain orientations in the shearing plane. The major axis of the order parameter tensor **S** does not rotate from the vorticity direction, since there is no symmetry-breaking disturbance to tell it which direction to move; instead, **S** is distorted so severely that its major axis—initially oriented along the vorticity direction—is compressed into a minor axis, while a new major axis is stretched into existence by the strong shearing field that enlarges an eigenvalue of **S** corresponding to orientation in the shearing plane. At $\Gamma = 18$, the final state obtained is a wagging solution, while $\Gamma = 40$ resides in the regime of steady-state orientation.

The transitions discussed above are summarized in the stability diagram of Figure 9. On this diagram, the solid lines denote attracting states; these are tumbling, wagging, flow aligning, log-rolling, and kayaking states. The dashed lines denote unstable states; small perturbations from these states tend to grow. The diagram contains two bifurcation

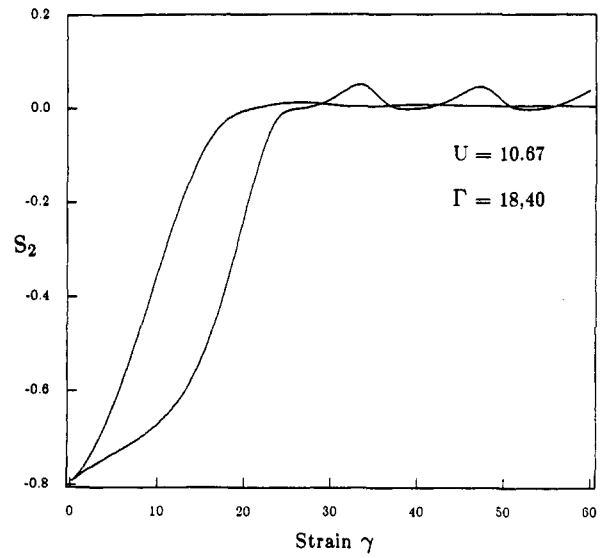

Figure 8. S_2 versus shear strain γ for $U = 10.67$ and an initial director angle ϕ of −90°, for Γ of 18 (oscillating line) and 40 (monotonic line).

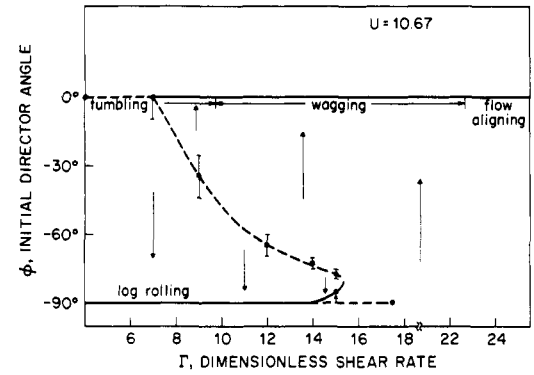

Figure 9. Stability diagram for $U = 10.67$; see text for details.

points; at one of these, with $\Gamma \approx 7$, an unstable tumbling state branches into a stable tumbling state and an unstable kayaking state. At the other bifurcation point, with $\Gamma \approx 14$, a stable log-rolling state bifurcates into an unstable log-rolling state and a stable kayaking state. There is also a turning point at $\Gamma \approx 15.5$, where a stable kayaking state becomes an unstable one. Finally, there is a termination point at $\Gamma \approx 18$, where the unstable log-rolling state disappears altogether. The error bars denote the accuracy of our determination of the locations of these states.

The overall picture, summarized in Figure 9, is unusual and rich in transitions. Since small changes in shear rate and orientation can produce such remarkable changes in molecular dynamics, a careful examination of the numerical accuracy of our spherical-harmonic solution technique is called for. By varying the time-step size, we can easily show that our Runge–Kutta integration is extremely accurate; thus, the most important source of error in the method, apart from replacement of $\hat{D}_r(\mathbf{u})$ by $\overline{D}_r$, is that the infinite series of spherical-harmonic functions required for a completely exact result is cut off at a finite number. Figure 10, however, shows that, at $U = 10.67$, very rapid convergence is achieved as the cutoff, l_{max}, is increased. A precise definition of l_{max} can be found in Appendix A. Note in Figure 10 that a large qualitative change is obtained when l_{max} is increased from 8 to 12, but *no visible change* occurs when l_{max} is further increased to $l_{max} = 16$. Thus our numerical technique is characterized by an unusually rapid rate of convergence, possibly an exponential one, as l_{max} is increased. Because of Figure 10, and several other tests like it, we are convinced that, for $U = 10.67$ and Γ

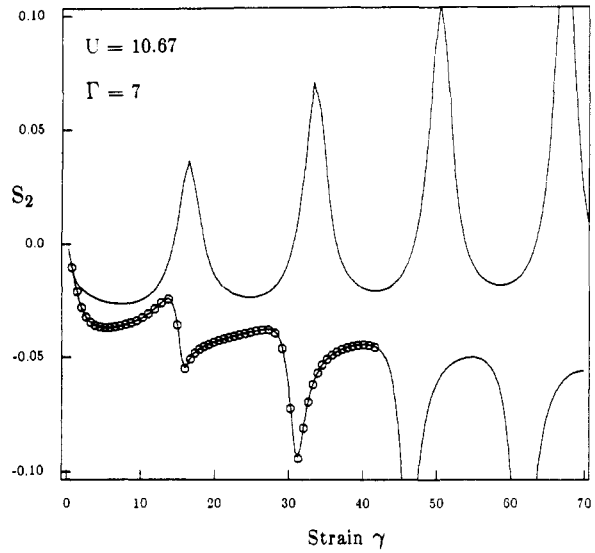

Figure 10. S_2 versus shear strain γ for $\Gamma = 7$ and $U = 10.67$ with an initial director angle ϕ of $-45°$, and $l_{max} = 8$ (upper curve), 12 (lower curve), and 16 (symbols).

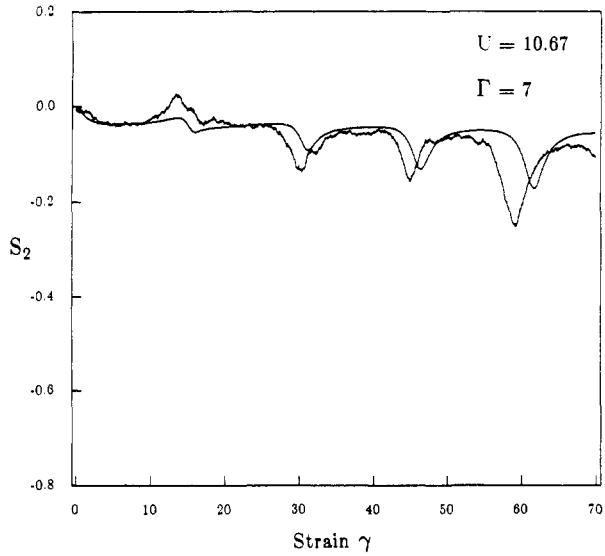

Figure 11. S_2 versus shear strain γ for $\Gamma = 7$ and $U = 10.67$ with an initial director angle ϕ of $-45°$ with $S^{eq} = 0.792$; the smooth line is from the spherical-harmonic technique, while the ragged line is from the stochastic method using $\bar{D}_r$ for the rotary diffusivity.

≤ 25, almost exact results are obtained for $l_{max} = 12$. Even the stable kayaking orbit at $\Gamma = 15$ remains unchanged when l_{max} is increased from 12 to 16.

2. Results for $U = 10.67$ with Unaveraged Rotary Diffusivity. Of course, even if our results are unaffected by the cutoff in l at l_{max}, we must still worry about our use of an averaged rotary diffusivity $\bar{D}_r$, instead of the more exact $\hat{D}_r(\mathbf{u})$. We here check this approximation by using the stochastic solution method described in Appendix B. First, however, we compare the two techniques for a case in which they should be the same. Figure 11 compares the solution obtained with the stochastic method with that obtained from the truncated spherical-harmonic expansion for $U = 10.67$, $\Gamma = 7$, and $\phi = -45°$, with the rotary diffusivity equal to $\bar{D}_r$ in *both* techniques. Although in the stochastic method we use an ensemble of 10 000 molecules, fluctuations are still significant and produce a noisy response. Also, the orbital period in the stochastic method is somewhat smaller than in the spherical-harmonic technique; this may be due to the finite size of the time step used in the former technique; see section II.B.2. Nevertheless, the results from the two methods are similar; in particular, both show a slow drift, superimposed on the regular oscillation, of the birefringence axis toward the log-rolling state.

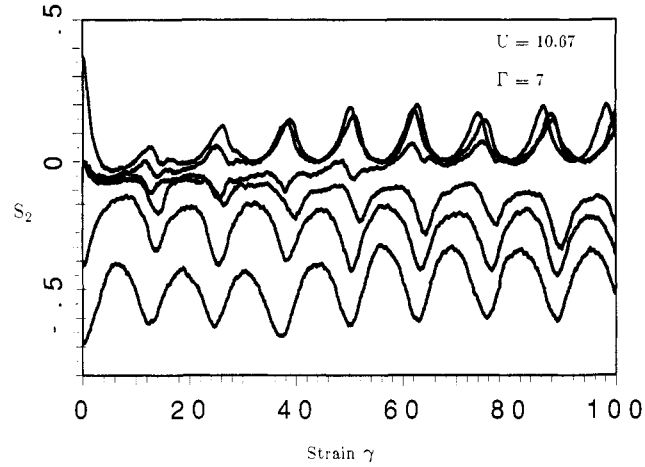

Figure 12. $S_2 \equiv S_{zz} - S_{yy}$ versus shear strain γ for $\Gamma = 7$ and $U = 10.67$ predicted by the stochastic method using $\hat{D}_r$ for the rotary diffusivity. For the upper curve, $\phi = -30°$, while for the lower two curves $\phi = -60°$ and $-75°$. The three curves that begin at $S_2 = 0$ are obtained using $\phi = -45°$ and three different initial distribution functions for which $S^{eq} = 0.732$ (uppermost of the three), 0.756 (middle of the three), and 0.792 (bottommost of the three).

The stochastic method with the unaveraged rotary diffusivity $\hat{D}_r(\mathbf{u})$ instead of $\bar{D}_r$ shows that, for $U = 10.67$ and $\Gamma = 7$, *either the shearing plane or the vorticity axis can be the attractor*, depending on the initial state; see Figure 12. For the stochastic method we prepared different starting states in two different ways. In the first way, we ran a simulation with $\Gamma = 0$, letting Brownian motion prepare a typical equilibrium distribution function. For a time step of $\Delta t = 0.005$, the value of S^{eq} in ensembles typical of equilibrium fluctuates between about 0.72 and 0.76. The fluctuations occur because the ensemble, though large, is finite. Note also that the range of values of S^{eq} is lower than the nearly exact value, $S^{eq} = 0.792$, found with the spherical-harmonic method. This difference occurs because there is a significant finite time-step size effect in the stochastic calculations; as Δt is decreased, the average value of S^{eq} increases and approaches the correct value. Computationally, however, $\Delta t = 0.005$ is the smallest time step we can afford at present. Thus we prepare one initial condition by taking a typical configuration of rods achieved during the run in which $\Gamma = 0$; for this typical configuration, $S^{eq} = 0.732$. We obtain a set of different initial conditions from this one by uniformly rotating all rods to obtain a desired initial director orientation; here we consider the four initial angles $\phi = -30°, -45°, -60°$, and $-75°$. Obviously, $S^{eq} = 0.732$ for all angles in this set of initial conditions.

A second set of initial conditions was prepared by choosing different configurations from the equilibration run. Because of fluctuations, we were able to find not only the configuration mentioned above for which $S^{eq} = 0.732$ but also one for which $S^{eq} = 0.756$. We produced a third configuration, one that has the correct value of the scalar order parameter—namely, $S^{eq} = 0.792$, by rotating "by hand" some of the rods in the ensemble with $S^{eq} = 0.756$. In this way we completed a second set of initial configurations, with $S^{eq} = 0.732, 0.756$, and 0.792; for each member of this second set, we choose $\phi = -45°$. Because of fluctuations, we also needed to impose an additional, small, deformation on these three initial configurations to satisfy the condition $S_2 = 0$; this condition would hold for an infinite ensemble with $\phi = -45°$.

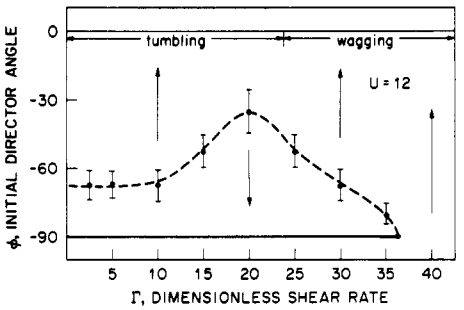

Figure 13. Stability diagram for $U = 12$. Not shown is the flow-aligning regime that exists for $\Gamma \gtrsim 85$.

Figure 12 shows the results of the stochastic method for both sets of initial conditions described above, with $U = 10.67$, $\Gamma = 7$. Note that, for $\phi = -30°$, the birefringence axis quickly moves toward the tumbling state in the shearing plane, while, for $\phi = -60°$, it drifts slowly toward the vorticity axis. For $\phi = -75°$, it drifts up a bit and seems to converge with the results for $\phi = -60°$. Thus for this value of U and of Γ, there seem to be two attractors, the tumbling state in the shearing plane and a kayaking state. When ϕ is held fixed at $-45°$, the direction that the birefringence axis drifts depends on the initial distribution of rod orientations. For the most sharply peaked orientation distribution with $S^{eq} = 0.792$, there is a drift toward the vorticity axis, while for the less sharply peaked distributions, with $S^{eq} = 0.732$ and 0.756, the migration is toward the shearing plane. The results are consistent with what we found for the spherical-harmonic technique, in that when the tumbling plane is an attractor, it is typically a strong one, while log-rolling or kayaking orbits are at best weak attractors. However, the results of the stochastic method with unaveraged $\hat{D}_r(\mathbf{u})$ differ from those of the spherical-harmonic method, in that, at $U = 10.67$ and $\Gamma = 7$, the latter method predicts that the only attractor is the log-rolling state, while the stochastic method predicts the existence of two stable attractors. Also, when the unaveraged $\hat{D}_r(\mathbf{u})$ is used instead of $\bar{D}_r$, the period of the oscillation decreases from 15 to around 12. We have seen this effect repeatedly; thus the preaveraging of $\hat{D}_r(\mathbf{u})$ apparently increases somewhat the tumbling period.

Despite these differences between the results for the two techniques, they are consistent in that they predict that *orientation states outside the shearing plane can be attractors* for the birefringence axis and that, for some values of concentration and shear rate, *there can be two coexisting attractors*. Since we have obtained these results using two refined methods of solving the Doi equations, we are confident that they represent the true mathematical behavior of the Doi theory. Of course, there are *physical* approximations involved in the Doi theory that could, in principle, make the results presented here uncharacteristic of real systems; an investigation of this possibility is, however, beyond the scope of the present effort.

3. Results for $U = 12$ and $U = 14$. Finally, we address the question of the sensitivity of our results to the strength of the nematic potential. Figure 13 shows the stability diagram obtained from the spherical-harmonic technique with l_{max} for $U = 12$. It is similar to that for $U = 10.67$ in that, above a critical value Γ_c of Γ, the shearing plane is the only attractor for the birefringence axis, while for a range of Γ below this value both the shearing plane and the vorticity axis are attractors. Results for $U = 12$ are also similar to those for $U = 10.67$ in that, as Γ is decreased below Γ_c, an increasing range of initial director angles lies within the domain of attraction of the vorticity axis. However, for $U = 12$, the shearing plane remains an attractor for values of Γ as low as $\Gamma = 2$, while for $U = 10.67$, only the vorticity axis is an attractor when $\Gamma \leq 7$, at least according to the spherical-harmonic method.

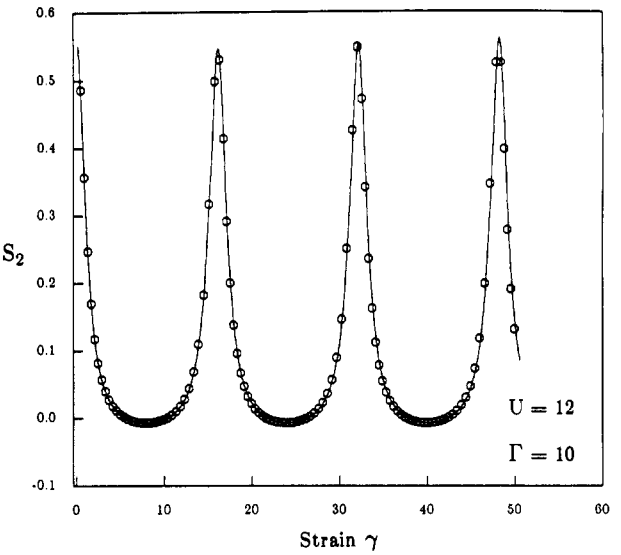

Figure 14. S_2 versus shear strain γ for $\Gamma = 10$ and $U = 12$ with an initial director angle ϕ of $-24.55°$; $l_{max} = 12$ (curve) and 16 (symbols).

The critical values of the dimensionless shear rate are $\Gamma_c \approx 15.5$ for $U = 10.67$ and $\Gamma_c \approx 36$ for $U = 12$. However, if we define the Deborah number by $De \equiv \dot{\gamma}\tau$, where $\tau \equiv 1/6\bar{D}_r^{eq}$ is the equilibrium (no-flow) rotational relaxation time, then we obtain $De = \dot{\gamma}/6\bar{D}_r^{eq} = \Gamma D_r/6\bar{D}_r^{eq}$. Now, for $U = 10.67$, $\bar{D}_r^{eq}/D_r = 3.129$, while for $U = 12$, $\bar{D}_r^{eq}/D_r = 4.422$. Thus the shearing plane becomes the only attractor at $De \approx 0.83$ when $U = 10.67$, and, for $U = 12$, it becomes the only attractor at $De \approx 1.36$.

Thus, except possibly at the lowest values of Γ, the results for $U = 12$ are qualitatively similar to those for $U = 10.67$. Even at low Γ, the results for these two values of U are similar in that all orbits are close to marginal stability, and hence any drift toward either attractor is slow. It is also possible, based on our calculations with the stochastic method, that the disappearance of the shearing plane as an attractor at low Γ for $U = 10.67$ is an artifact of the replacement of $\hat{D}_r$ by $\bar{D}_r$ and that the true behavior for $U = 10.67$ at low Γ is similar to that for $U = 12$.

Figure 14 compares a solution for $U = 12$ and $\Gamma = 10$ obtained with $l_{max} = 12$ with the more refined result for this problem when $l_{max} = 16$. As is true for $U = 10.67$, there is little difference between these calculations, which shows that $l_{max} = 12$ is high enough to give a nearly converged result. For $U = 14$, however, Figure 15 shows that results for $l_{max} = 12$ disagree qualitatively from those for $l_{max} = 16$. For $l_{max} = 12$, the birefringence axis is attracted toward the shearing plane, while for $l_{max} = 16$ it drifts toward the vorticity axis. A detailed inspection of the runs plotted in Figure 14 shows that for $U = 12$ there is also a difference, albeit slight, between runs for $l_{max} = 12$ and $l_{max} = 16$ and that this difference is in the same direction as the much larger difference evident in Figure 15. That is, for $U = 12$, the birefringence axis drifts less rapidly toward the vorticity axis for $l_{max} = 12$ than for $l_{max} = 16$, but this drift is so slight that it is not observable in Figure 14 and does not qualitatively change the conclusion that the birefringence axis drifts toward the vorticity axis. For $U = 14$, however, the difference between results for $l_{max} = 12$ and $l_{max} = 16$ is large enough to change the direction of the drift in the birefringence axis, and thus when $U = 14$, the calculations for $l_{max} = 12$ are untrustworthy.

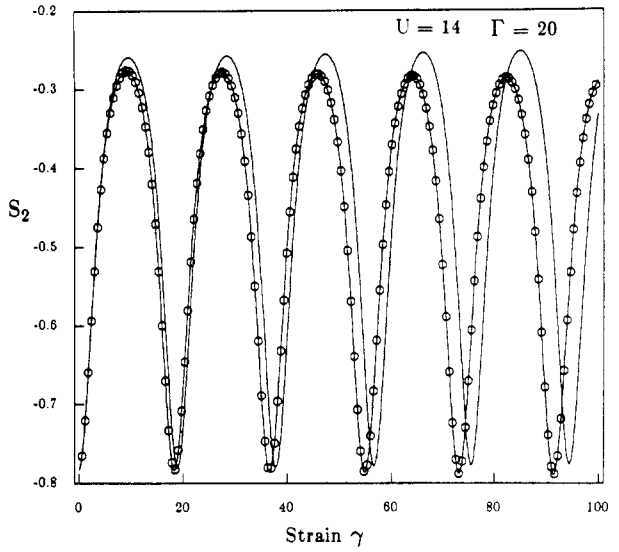

Figure 15. S_2 versus shear strain γ for $\Gamma = 20$ and $U = 14$ with an initial director angle ϕ of $-75°$; $l_{max} = 12$ (curve) and 16 (curve with symbols).

Table I
Computed Values of S^{eq}

U, strength of potential	$l_{max} = 12$	$l_{max} = 16$
10.67	0.7920	0.7920
12	0.8555	0.8556
14	0.9233	0.9042

It is not surprising that the accuracy of the spherical-harmonic technique with fixed l_{max} is degraded when U is increased, when one considers how the equilibrium order parameter S^{eq} increases with increasing U, as seen in Table I. As S^{eq} increases, the orientation distribution function ψ becomes more sharply peaked, and one must use higher order spherical-harmonic functions to represent it. While we will not here present extensive refined calculations with $l_{max} = 16$ for $U = 14$, it is worth noting from the one refined run that we have that the vorticity axis can be the attractor for $U = 14$ also. We also note that, in contrast to the spherical-harmonic technique, the accuracy of the stochastic method should not decrease, but if anything improve, when U is increased, since the fluctuations that limit the accuracy of the stochastic method presumably become less important as U increases and the distribution function becomes more sharply peaked. For the same reason, at higher values of U we expect less loss of accuracy when $\hat{D}_r$ is replaced by $\overline{D}_r$.

III. Discussion and Summary

Two different refined numerical solution methods for solving the time-dependent molecular orientation distribution function ψ of the monodomain Doi theory have shown that nonlinear molecular viscoelastic effects at modest Deborah number act to stabilize both orientations in the shearing plane and either log-rolling orientations that are orthogonal to that plane or kayaking orbits that are skewed with respect to the shearing plane. One of these methods, the spherical-harmonic method, uses a rotary diffusivity $\overline{D}_r$ that is the same for all molecules but varies with ψ; in the other, the stochastic method, the rotary diffusivity $\hat{D}_r(\mathbf{u})$ depends on the instantaneous orientation $\mathbf{u}$ of each molecule and varies from molecule to molecule in the ensemble. We have computed stability diagrams for $U = 10.67$ and $U = 12$ using the spherical-harmonic method; these diagrams show that, over a significant range of shear rates, both log-rolling and in-plane tumbling or wagging solutions can be stable at the same shear rate. The predictions of the two different numerical techniques differ in the range of shear rates over which two orientational states can both be stable and in that, when the unaveraged $\hat{D}_r(\mathbf{u})$ is used, the period of the tumbling orbit is shorter. While stable kayaking solutions are rarely found in results obtained using the spherical-harmonic method, they might be more common with the stochastic method.

We are confident that the observed stabilization of two different orientational states reflects the true behavior of the Doi theory; however, we must be cautious about applying these predictions to real liquid-crystalline polymers. Several idealizations are involved in the Doi theory, including perfect rigidity and monodispersity of the molecules, a mean-field "cage" model for the rod dynamics, and a mean-field excluded-volume potential, which here is taken to be that of Onsager. More importantly, however, we have not considered the effects of director gradients or texture. Experiments on lyotropic liquid-crystalline polymers have shown that, even when the sample starts out as a monodomain, usually shearing quickly introduces pervasive orientational inhomogeneities. Thus, our monodomain calculations cannot apply to an entire bulk sample but only to individual domains that remain nearly homogeneously oriented within the bulk. These domains experience not only the viscous and molecular elastic effects included in our calculations but also the effects of director gradients which we have neglected.

The neglect of director gradients—i.e., interdomainal interactions—is probably reasonable at moderate and high shear rates, as evidenced by the good agreement of the predictions of the monodomain Doi theory with measured values of the first and second normal stress differences N_1 and N_2, at shear rates above the value at which N_1 changes sign from positive to negative.[15] At shear rates below this value, in calculations *that restrict the birefringence axis to the shearing plane*, the signs of N_1 and N_2 are correctly predicted by the theory, but the shear rate dependence predicted for N_1 seems to be stronger than observed, and the ratio $-N_2/N_1$ is incorrectly predicted to increase without bound as the shear rate decreases.[9] In the measurements at low shear rates, $-N_2/N_1$ appears to remain fixed at a value of about 0.5.[15] While these discrepancies may be caused by the neglect of director gradients, it is possible that the restriction of the birefringence axis to the shearing plane is also at least partially responsible.

The simulations presented here allow us to begin to assess the effects of out-of-plane orientations on N_1 and N_2. Light and X-ray scattering on lyotropic[28,29] and thermotropic[30] LCP's show that at low shear rates the domain orientation distribution is only slightly distorted from isotropy. Thus at low shear rates it is more reasonable to compute N_1 and N_2 values from averages of the tumbling and log-rolling states than to obtain these values from the tumbling states alone. The time-averaged values of N_1 and N_2 for the in-plane tumbling and wagging states over this range of shear rates were presented earlier;[9] at shear rates below $\Gamma = 9$, N_2 is negative while N_1 is positive. Figure 16 shows the predictions of N_1 and N_2 obtained for the stable log-rolling states for $U = 10.67$; for the log-rolling states, N_1 and N_2 are *both positive*, and $N_2/N_1 \sim 0.23$ is nearly independent of shear rate. The values of N_1 and N_2 in the log-rolling state at a given Γ turn out to be comparable in magnitude to their counterparts in the tumbling or wagging states at the same Γ. Thus an average of the log-rolling and tumbling values of N_2 that reflects the relative preponderance of these two states in the textured fluid would presumably be *less negative* than the value of N_2 obtained from the tumbling state alone,

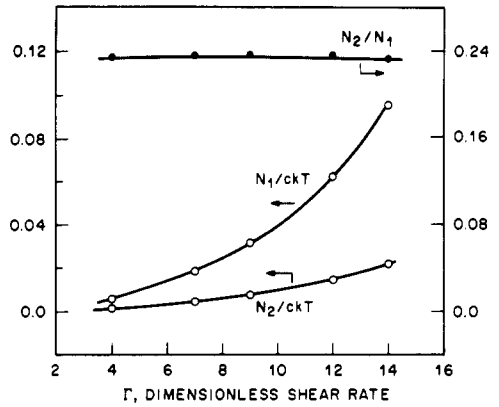

Figure 16. N_1, N_2, and N_2/N_1 as functions of Γ for $U = 10.67$ in the log-rolling state.

and the ratio $-N_2/N_1$ would be brought closer to the experimental value.

Our predictions show that, in many cases, after prolonged shearing there should be a coexistence of two distinct states: the tumbling (or wagging) and the log-rolling (or kayaking) states. The shearing time required to produce these distinct states is predicted to become enormous, perhaps thousands of strain units or even more, as the shear rate is reduced. An initially nearly isotropic domain orientation distribution would therefore remain nearly isotropic even under prolonged shearing, which is consistent with the X-ray and light scattering studies cited above.

As the shear rate is increased, however, the simulations predict that the time required for domains to find their way to the tumbling attractor is greatly reduced while the time required to reach the log-rolling attractor is somewhat reduced. Thus, after a few hundred strain units of shear applied to an initially isotropic distribution of domain orientations, we expect to see the coexistence of tumbling states with log-rolling and/or kayaking states, and, indeed, in recent light scattering studies on sheared lyotropic LCP's,[28,29] it was observed that, above a critical shear rate $\dot{\gamma}_c$, H_V (or V_H) polarized light scattering undergoes a drastic change. The incident beam in these experiments is in the z direction, that is, normal to the surfaces between which the sample is sheared. Below $\dot{\gamma}_c$, the scattering pattern in the x–y plane shows only a modest distortion from circular symmetry, as mentioned above. Here x is the flow direction and y is perpendicular to x and z. Above $\dot{\gamma}_c$, a profound change occurs; a narrow streak parallel to y appears; superimposed on this structure is an "X" or four-lobed "butterfly" pattern, with each lobe oriented at an angle somewhat greater than 45° with respect to the y axis. It is natural to suggest, with Takebe et al.,[29] that these two superposed structures (the streak and the butterfly) reflect the existence of two types of coherent molecular arrangement in the flowing LCP's. The narrow streak is readily interpreted to be caused by coherent spatial regions in which the molecular orientation is primarily in the flow (or x) direction. This orientational state could represent the domains undergoing collective tumbling, since tumbling domains spend most of their time oriented at angles close to the flow direction. The butterfly pattern is not so readily interpreted, but the structure that produces it probably involves director orientations that are not parallel to the flow and may represent kayaking domains. If these are kayaking domains, perhaps their orientation would become more nearly perpendicular to the flow direction if the shear were to be maintained for the thousands of strain units that the theory shows are required.

The above explanation of the butterfly pattern must be regarded as speculative, and alternative viewpoints are provided by Takebe et al.[29] and Picken et al.[31] If, however, two kinds of orientational states do coexist in sheared LCP's, these might be implicated in the observations of formation of bands orthogonal to the flow direction after cessation of shear.[28,32] Recent experimental work shows that there is a critical Deborah number required to create the texture that will lead to band formation after shearing ceases[17,28] and that, near the critical shear rate, hundreds or even thousands of strain units must be imposed if this texture is to form. If log-rolling or kayaking domains are part of the texture required for band formation, then the large strains required for band formation could be explained by our calculations.

Acknowledgment. This work was motivated by G. Marrucci, W. Burghardt, and S. Patel, all of whom independently suggested the importance of studying out-of-plane initial director orientations. H.C.Ö. thanks the Swiss National Foundation for Scientific Research (Grant No. 21-29571.90) for financial support. The simulations using the stochastic method were carried out on the Swiss Federal Institute of Technology's Cray XMP computer.

Appendix A: Spherical-Harmonic Numerical Technique

Equation of Change of Orientational Order. The Doi equation for the orientational distribution function $\psi(\mathbf{u})$ that we wish to solve is given by eq 1 and 2. As described earlier,[9,22] our approach is to expand the distribution function ψ in terms of the spherical-harmonic functions Y_l^m. We define x as the flow direction of the simple shearing flow, z as the direction of the gradient of the flow, and y as the vorticity direction. In earlier work, it was assumed that the distribution function was symmetric with respect to the x–z plane. This means that the nematic director must lie in the x–z plane. Here, we relax this assumption. Therefore we express ψ as

$$\psi(\mathbf{u},t) = \sum_{\substack{l=0 \\ l=\text{even}}}^{\infty} \sum_{m=-l}^{l} b_{lm} Y_{lm} \tag{A1}$$

and we allow the coefficients b_{lm} to be complex. When ψ has symmetry about the x–z plane, each b_{lm} is real. Since $Y_{l,-m} = (-1)^m Y^*_{l,m}$, we insure that ψ is real by imposing the requirement that

$$b_{l-m} = (-1)^m b^*_{lm} \tag{A2}$$

The asterisk denotes a complex conjugate. Requirement (A2) also holds when ψ is symmetric about the x–z plane, i.e., when the b_{lm}'s are real. The restriction to even values of l is a reflection of the even parity of ψ, namely, that $\psi(-\mathbf{u}) = \psi(\mathbf{u})$.

We define the inner product

$$\langle lm|X\rangle \equiv \int Y^*_{lm} X \, du^2 \tag{A3}$$

where X is some expression involving ψ. Now, multiplying eq 1 by Y^*_{lm} and integrating over the unit sphere gives

$$\frac{\partial}{\partial t}\langle lm|\psi\rangle = -\left\langle lm\left|\frac{\partial}{\partial \mathbf{u}}\cdot\{[\mathbf{u}\cdot\nabla\mathbf{v} - \mathbf{uuu}:\nabla\mathbf{v}]\psi\}\right.\right\rangle + \bar{D}_r\left\langle lm\left|\frac{\partial}{\partial \mathbf{u}}\cdot\frac{\partial}{\partial \mathbf{u}}\psi\right.\right\rangle + \frac{\bar{D}_r}{kT}\left\langle lm\left|\frac{\partial}{\partial \mathbf{u}}\cdot\left[\psi\frac{\partial}{\partial \mathbf{u}}V_{ev}\right]\right.\right\rangle \tag{A4}$$

Equation A4 is a set of complex equations for the complex

coefficients b_{lm}. Because of condition (A2), we need only solve these equations for $m \geq 0$.

Before we can solve eq A4, we must evaluate $\bar{D}_r$ and the inner products in terms of the b_{lm}'s. An expressions for $\bar{D}_r$ is obtained by generalizing that given by Doi and Edwards[33] to complex b_{lm}:

$$\bar{D}_r = D_r\left(1 - 8\pi \sum_{\substack{l=2 \\ l=\text{even}}}^{\infty} \sum_{m=-l}^{l} \left(\frac{l-1}{l+2}\right)\left[\frac{(l-3)!!}{l!!}\right]^2 |b_{lm}|^2\right)^{-2} \tag{A5}$$

Here

$$|b_{lm}|^2 \equiv b_{lm} b_{lm}^* \tag{A6}$$

and

$$n!! \equiv \begin{cases} n(n-2)(n-4)...(1), & \text{for } n = \text{odd} \\ n(n-2)(n-4)...(2), & \text{for } n = \text{even} \\ 1, & \text{for } n \leq 1 \end{cases} \tag{A7}$$

Two of the inner products in eq A4 can be readily evaluated (see Doi and Edwards[33]):

$$\langle lm|\psi\rangle = b_{lm} \tag{A8}$$

$$\left\langle lm\left|\frac{\partial}{\partial \mathbf{u}}\cdot\frac{\partial}{\partial \mathbf{u}}\psi\right.\right\rangle = -l(l+1)b_{lm} \tag{A9}$$

Here, use has been made of the orthonormality of the Y_{lm}: $\langle lm|l'm'\rangle = \delta_{ll'}\delta_{mm'}$, where $\delta_{ij} = 1$ if $i = j$ and $\delta_{ij} = 0$ if $i \neq j$.

To evaluate the convection inner product in eq A4, for simple shear with flow in the x direction and gradient in the z direction, we write $(\partial/\partial \mathbf{u})\cdot\{[\mathbf{u}\cdot\nabla\mathbf{v} - \mathbf{uuu}:\nabla\mathbf{v}]\psi\}$ as $\dot{\gamma}\bar{\Gamma}\psi$ where $\dot{\gamma}$ is the shear rate and $\bar{\Gamma}$ is

$$\bar{\Gamma} = \cos^2\theta\cos\phi\frac{\partial}{\partial\theta} - \cot\theta\sin\phi\frac{\partial}{\partial\phi} - 3\sin\theta\cos\theta\cos\phi \tag{A10}$$

Here the polar and azimuthal angles θ and ϕ are defined in such a way that

$$u_x = \sin\theta\cos\phi; \quad u_y = \sin\theta\sin\phi; \quad u_z = \cos\theta \tag{A11}$$

$\bar{\Gamma}$ can be written in terms of spherical-harmonic functions and the angular momentum operators. The angular momentum operators L_α are defined by[34]

$$L_\alpha \equiv -i\left(\mathbf{u}\times\frac{\partial}{\partial\mathbf{u}}\right)_\alpha; \quad \alpha = x, y, z \tag{A12}$$

Here i is the imaginary unit. $\bar{\Gamma}$ is then given by

$$\bar{\Gamma} = (16\pi/45)^{1/2}Y_2^0 iL_y + \frac{i}{3}L_y + (2\pi/15)^{1/2}(Y_2^1 + Y_2^{-1})L_z - 3(2\pi/15)^{1/2}(-Y_2^1 + Y_2^{-1}) \tag{A13}$$

This expression corrects the sign errors in eq B.1 of Doi and Edwards.[33]

To assist in our evaluation of the inner products, we use the definitions

$$L_+ \equiv L_x + iL_y; \quad L_- \equiv L_x - iL_y \tag{A14}$$

We define the shorthand

$$[l,m,p,q,l']^- \equiv \sum_{m'=0}^{l'} \langle lm|Y_p^q(L_+ - L_-)|l'm'\rangle b_{l'm'}$$

$$[l,m,p,q,l']^+ \equiv \sum_{m'=0}^{l'} \langle lm|Y_p^q(L_+ + L_-)|l'm'\rangle b_{l'm'}$$

$$[l,m,p,q,l']^z \equiv \sum_{m'=0}^{l'} \langle lm|Y_p^q L_z|l'm'\rangle b_{l'm'}$$

$$[l,m,p,q,l']^0 \equiv \sum_{m'=0}^{l'} \langle lm|Y_p^q|l'm'\rangle b_{l'm'} \tag{A15}$$

Here $|l'm'\rangle$ denotes $Y_{l'm'}$ and the angular momentum operators act on $|l'm'\rangle$, as is the usual convention. These operators can be eliminated using the following identities:[34]

$$L_z|l'm'\rangle = m'|l'm'\rangle$$

$$L_+|l'm'\rangle = [l'(l'+1) - m'(m'+1)]^{1/2}|l'm'+1\rangle$$

$$L_-|l'm'\rangle = [l'(l'+1) - m'(m'-1)]^{1/2}|l'm'-1\rangle \tag{A16}$$

In terms of the above, we find the convection inner product is

$$-\frac{1}{\dot{\gamma}}\left\langle l,m\left|\frac{\partial}{\partial\mathbf{u}}\cdot\{[\mathbf{u}\cdot\nabla\mathbf{v} - \mathbf{uuu}:\nabla\mathbf{v}]\psi\}\right.\right\rangle = -\langle l,m|\bar{\Gamma}\psi\rangle =$$

$$\sum_{\substack{l'=0 \\ l'=\text{even}}}^{\infty} \{\frac{1}{2}(16\pi/45)^{1/2}[l,m,2,0,l']^- + \frac{1}{6}(4\pi)^{1/2}[l,m,0,0,l']^- +$$

$$(2\pi/15)^{1/2}[l,m,2,1,l']^z + (2\pi/15)^{1/2}[l,m,2,-1,l']^z +$$

$$3(2\pi/15)^{1/2}[l,m,2,1,l']^0 - 3(2\pi/15)^{1/2}[l,m,2,-1,l']^0\} \tag{A17}$$

Using the identities (A16), all inner products above can easily be reduced to the form $\langle lm|Y_p^q|l'm'\rangle$. A formula for $\langle lm|Y_p^q|l'm'\rangle$ is given by Messiah.[34]

We next evaluate the inner product in eq A4 that involves the excluded-volume potential. Integrating this term by parts gives

$$\left\langle lm\left|\frac{\partial}{\partial\mathbf{u}}\cdot\left[\psi\frac{\partial}{\partial\mathbf{u}}V_{ev}\right]\right.\right\rangle = \int\langle lm|\frac{\partial}{\partial\mathbf{u}}\cdot\left[\psi\frac{\partial}{\partial\mathbf{u}}V_{ev}\right]du^2 =$$

$$-\int\frac{\partial}{\partial\mathbf{u}}[\langle lm|]\cdot\psi\frac{\partial}{\partial\mathbf{u}}V_{ev}\,du^2 \tag{A18}$$

Next we invoke the identity

$$\left(\mathbf{u}\times\frac{\partial}{\partial\mathbf{u}}f\right)\cdot\left(\mathbf{u}\times\frac{\partial}{\partial\mathbf{u}}g\right) = \left(\frac{\partial}{\partial\mathbf{u}}f\right)\cdot\left(\frac{\partial}{\partial\mathbf{u}}g\right) \tag{A19}$$

where f and g are arbitrary functions of $\mathbf{u}$. Making use of this identity, eq A18 can be rewritten as

$$\left\langle lm\left|\frac{\partial}{\partial\mathbf{u}}\cdot\left[\psi\frac{\partial}{\partial\mathbf{u}}V_{ev}\right]\right.\right\rangle = -\int\mathbf{u}\times\frac{\partial}{\partial\mathbf{u}}[\langle lm|]\cdot\psi\mathbf{u}\times\frac{\partial}{\partial\mathbf{u}}V_{ev}\,du^2 = \int L_x[\langle lm|]\psi L_x[V_{ev}]\,du^2 + \int L_y[\langle lm|]\psi L_y[V_{ev}]\,du^2 + \int L_z[\langle lm|]\psi L_z[V_{ev}]\,du^2 \tag{A20}$$

In the above, we have made use of eq A12.

In expression (2) for the Onsager potential, sin $(\mathbf{u},\mathbf{u}')$ can be written in terms of spherical-harmonic functions

as[33]

$$\sin(\mathbf{u},\mathbf{u}') = -2\pi^2 \sum_{\substack{l'=0\\ l'=\text{even}}}^{\infty} \sum_{m'=-l'}^{l'} \left(\frac{l'-1}{l'+2}\right)\left[\frac{(l'-3)!!}{l'!!}\right]^2 \times Y_{l'}^{m'}(\mathbf{u})\, Y_{l'}^{m'}(\mathbf{u}') \quad \text{(A21)}$$

Inserting eq A21 and expression (A1) for $\psi(\mathbf{u}')$ in terms of the spherical-harmonic functions into eq 2 and using the orthonormal properties of the spherical-harmonic functions give

$$V_{ev} = -2\pi^2 U \sum_{\substack{l'=0\\ l'=\text{even}}}^{\infty} \sum_{m'=0}^{l'} \left(\frac{l'-1}{l'+2}\right)\left[\frac{(l'-3)!!}{l'!!}\right]^2 b_{l'-m'}|l'm'\rangle \quad \text{(A22)}$$

Expanding the remaining ψ in eq A20 in terms of the spherical-harmonic functions Y_p^q and using eq A16 to eliminate the angular momentum operators yield, after some algebra

$$\left\langle lm\left|\frac{\partial}{\partial \mathbf{u}}\cdot\left[\psi\frac{\partial}{\partial \mathbf{u}}V_{ev}\right]\right\rangle = -2\pi^2 U \sum_{\substack{p=0\\ p=\text{even}}}^{\infty} \sum_{q=-p}^{p} \sum_{\substack{l'=0\\ l'=\text{even}}}^{\infty} \sum_{m'=-l'}^{l'} b_{pq} \times \left(\frac{l'-1}{l'-2}\right)\left[\frac{(l'-3)!!}{l'!!}\right]^2 (-1)^{m'} b_{l'-m'}\{-mm'\langle lm|pq|l'm'\rangle - \frac{1}{2}[l(l+1)-m(m+1)]^{1/2}[l'(l'+1)-m'(m'+1)]^{1/2} \times \langle lm+1|pq|l'm'+1\rangle - \frac{1}{2}[l(l+1)-m(m-1)]^{1/2} \times [l'(l'+1)-m'(m'-1)]^{1/2}\langle lm-1|pq|l'm'-1\rangle\} \quad \text{(A23)}$$

Expressions for the Birefringence and Stress Tensors. Once eq A4 is solved for the coefficients b_{lm} by Runge–Kutta integration as described in ref 22, the birefringence and stress tensors can be evaluated. The ij component of the birefringence tensor is proportional to ν times the following tensor $\mathbf{S}_{ij}$

$$\mathbf{S}_{ij} \equiv \left\langle u_i u_j - \frac{1}{3}\delta_{ij}\right\rangle \equiv \int \psi\left(u_i u_j - \frac{1}{3}\delta_{ij}\right) du^2 \quad \text{(A24)}$$

where the broken brackets "⟨ ⟩" denote an average over ψ.

Using eq A11, a tabulation of spherical-harmonic functions in ref 34, the fact that $b_{l-m} = (-1)^m b_{lm}^*$, and the orthonormal property of spherical-harmonic functions, we obtain the expressions

$$\langle u_x u_z\rangle = -2(2\pi/15)^{1/2}\,\mathrm{Re}\,(b_{21})$$

$$\langle u_x^2 - u_z^2\rangle = (2\pi/15)^{1/2}(2\,\mathrm{Re}\,(b_{22}) - \sqrt{6}b_{20})$$

$$\langle u_z^2 - u_y^2\rangle = (2\pi/15)^{1/2}(2\,\mathrm{Re}\,(b_{22}) + \sqrt{6}b_{20})$$

$$\langle u_x u_y\rangle = -2(2\pi/15)^{1/2}\,\mathrm{Im}\,(b_{22})$$

$$\langle u_z u_y\rangle = -2(2\pi/15)^{1/2}\,\mathrm{Im}\,(b_{21}) \quad \text{(A25)}$$

where Re (X) and Im (X) denote the real and imaginary parts of X.

The viscoelastic stress tensor σ_{ij} can be obtained from the diffusive terms in eq 1:

$$\sigma_{ij} = -\frac{\nu kT}{2}\int \left(u_i u_j - \frac{1}{3}\delta_{ij}\right)\frac{\partial}{\partial \mathbf{u}}\cdot\left[\frac{\partial \psi}{\partial \mathbf{u}} + \psi\frac{\partial}{\partial \mathbf{u}}\left(\frac{V_{ev}}{kT}\right)\right] du^2 \quad \text{(A26)}$$

This produces two contributions to $\sigma_{ij} = \sigma_{ij}^{b} + \sigma_{ij}^{ev}$, the Brownian term σ_{ij}^{b} and the excluded-volume term σ_{ij}^{ev}. These are

$$\sigma_{ij}^{b} = -\frac{\nu kT}{2}\int \left(u_i u_j - \frac{1}{3}\delta_{ij}\right)\frac{\partial}{\partial \mathbf{u}}\cdot\frac{\partial \psi}{\partial \mathbf{u}}\, du^2 = 3\nu kT\left\langle u_i u_j - \frac{1}{3}\delta_{ij}\right\rangle = 3\nu kT\sigma_{ij} \quad \text{(A27)}$$

and

$$\sigma_{ij}^{ev} = -\frac{\nu kT}{2}\int \left(u_i u_j - \frac{1}{3}\delta_{ij}\right)\frac{\partial}{\partial \mathbf{u}}\cdot\psi\frac{\partial}{\partial \mathbf{u}}\left(\frac{V_{ev}}{kT}\right) du^2 \quad \text{(A28)}$$

Thus, σ_{ij}^{b} can be obtained from eq A25. To obtain σ_{ij}^{ev} most simply, we define

$$P_{lm} \equiv \frac{1}{kT}\left\langle lm\left|\frac{\partial}{\partial \mathbf{u}}\cdot\left[\psi\frac{\partial}{\partial \mathbf{u}}V_{ev}\right]\right\rangle \quad \text{(A29)}$$

According to eq A4, it is necessary to obtain P_{lm} to be able to solve the evolution equation for b_{lm}. Equation A23 gives an expression for P_{lm} which we can use to obtain σ_{ij}^{ev}. By analogy with eq A25, we obtain

$$\sigma_{xz}^{ev} = (2\pi/15)^{1/2}\,\mathrm{Re}\,(P_{21})$$

$$\sigma_{xx}^{ev} - \sigma_{zz}^{ev} = -(2\pi/15)^{1/2}\left(\mathrm{Re}\,(P_{22}) - \frac{1}{2}\sqrt{6}P_{20}\right)$$

$$\sigma_{zz}^{ev} - \sigma_{yy}^{ev} = -(2\pi/15)^{1/2}\left(\mathrm{Re}\,(P_{22}) + \frac{1}{2}\sqrt{6}P_{20}\right)$$

$$\sigma_{xy}^{ev} = (2\pi/15)^{1/2}\,\mathrm{Im}\,(P_{22})$$

$$\sigma_{zy}^{ev} = (2\pi/15)^{1/2}\,\mathrm{Im}\,(P_{21}) \quad \text{(A30)}$$

In the above derivation, we have corrected some typographical errors that appeared in ref 22. In particular, eq A17 includes a missing summation sign in Eq 24 of ref 22.

Appendix B: Stochastic Simulation Technique

From a mathematical point of view, the second-order partial differential equation (1) for $\psi = \psi(\mathbf{u},t)$ characterizes a Markovian stochastic process $\mathbf{U}(t)$. The range of the time-dependent random variable $\mathbf{U}(t)$ is the set of unit vectors in three dimensions, and $\psi(\mathbf{u},t)$ is the probability distribution for the random variable $\mathbf{U}(t)$. For the formulation of a simulation algorithm it is crucial that the above diffusion equation (or the Fokker–Planck equation) for the distribution function $\psi(\mathbf{u},t)$ is equivalent to a stochastic differential equation for the time evolution of the Markovian process $\mathbf{U}(t)$.[35] After discretizing the equivalent stochastic differential equation by introducing a finite time-step width Δt, one can derive the following evolution equation for the sequence of unit vectors $\mathbf{U}_j = \mathbf{U}(j\Delta t)$

$$\mathbf{U}_{j+1} = \frac{\mathbf{U}_j + \mathbf{f}(\mathbf{U}_j)\Delta t + (2\hat{D}_r(\mathbf{U}_j)\Delta t)^{1/2}\mathbf{W}_j}{|\mathbf{U}_j + \mathbf{f}(\mathbf{U}_j)\Delta t + (2\hat{D}_r(\mathbf{U}_j)\Delta t)^{1/2}\mathbf{W}_j|} \quad \text{(B1)}$$

where the deterministic contribution to the time evolution of $\mathbf{U}_j$ is given by

$$\mathbf{f}(\mathbf{u}) = \mathbf{u}\cdot\nabla\mathbf{v} - \frac{\hat{D}_r(\mathbf{u})}{kT}\frac{\partial V_{ev}}{\partial \mathbf{u}} + \frac{\partial \hat{D}_r(\mathbf{u})}{\partial \mathbf{u}} \quad \text{(B2)}$$

All the components of all the three-dimensional vectors $\mathbf{W}_j$ in eq (B1) are independent Gaussian random variables

with mean 0 and variance 1; that is

$$\langle \mathbf{W}_j \rangle = \mathbf{0}; \quad \langle \mathbf{W}_j \mathbf{W}_k \rangle = \delta_{jk}\delta \tag{B3}$$

Equation B1 is not of the standard form obtained by discretizing the stochastic differential equation equivalent to eq 1; it is rewritten in a way that guarantees that the constraint $|\mathbf{U}_j| = 1$ is strictly fulfilled for all finite time-step widths rather than only in the limit $\Delta t \to 0$, as is the case for the standard form (for $\Delta t \to 0$, the two discretizations are equivalent[36]).

The first and second terms in eq B2 represent the tendency of the rods to follow the applied flow field and the effect of the potential describing the interaction between rods, respectively; the potential force balances the frictional force resulting from a difference between rod and solvent velocities. The occurrence of the term $\partial \hat{D}_r(\mathbf{u})/\partial \mathbf{u}$ in eq B2 may be surprising. Such a term is required to reproduce the Boltzmann distribution at equilibrium, and it naturally appears when applying the formal rules of stochastic calculus.[35] Because the terms $(\Delta t)^{1/2}$ appear in eq B1, a systematic first-order calculation in Δt requires keeping track of second-order terms in the fluctuations $\mathbf{W}_j$. On the other hand, an amplitude of order $(\Delta t)^{1/2}$ for the Brownian fluctuations is crucial for obtaining a finite effect when many independent fluctuations (with random signs) are added, as is well-known for diffusive processes. Finally, the restriction to unit vectors, which in eq 1 is achieved by using the transverse projection operator $(\delta - \mathbf{uu})$ and the transverse gradient $\partial/\partial \mathbf{u}$, is in the stochastic evolution equation (B1), a trivial consequence of the normalization.

Equation B1 immediately yields a simulation algorithm for the model given by the diffusion equation (1), irrespective of the particular form of the rotational diffusion coefficient $\hat{D}_r$ and of the potential V_{ev}. Namely, starting from an initial unit vector $\mathbf{U}_0$ which may be chosen to be oriented completely at random or peaked around a particular direction, eq B1 can be used to generate a sequence of unit vectors $\mathbf{U}_j$, $j = 1, 2, \ldots$. In each step of the simulation, one needs three independent Gaussian random numbers. The resulting sequence $\mathbf{U}_j$ is one particular realization (or trajectory) of the stochastic process $\mathbf{U}(t)$ at the times $t_j = j\Delta t$; the average of an arbitrary quantity $\mathbf{A}(\mathbf{u})$ performed with the distribution function $\psi(\mathbf{u},t_j)$ of $\mathbf{U}_j$ can be obtained approximately from an ensemble of N_T trajectories, $\mathbf{U}_j^{(n)}$ with $n = 1, 2, \ldots, N_T$, as

$$\int \mathbf{A}(\mathbf{u})\, \psi(\mathbf{u},t_j)\, du^2 = \frac{1}{N_T}\sum_{n=1}^{N_T} \mathbf{A}(\mathbf{U}_j^{(n)}) \tag{B4}$$

where the statistical fluctuations of the arithmetic mean on the right side of this equation decrease with increasing N_T.

Because of the mean-field character of the Doi equation, the diffusion coefficient $\hat{D}_r$ and the potential V_{ev} themselves depend on averages of the stochastic process $\mathbf{U}(t)$. For each trajectory of the ensemble one thus has to calculate averages over all the trajectories in the ensemble, and the required computer time is hence proportional to N_T^2. Since we must approach the limit $N_T \to \infty$ to minimize errors due to the finite ensemble size, accurate simulations of the time-evolution equation are very expensive. For example, for the discussion of the stability of certain configurations, we used ensembles of $N_T = 10\,000$ trajectories, and a single time step then takes roughly 10 s on a Cray XMP computer.

Much more accurate simulations are possible for models in which $\hat{D}_r$ and V_{ev} do not depend on averages (or only on the same averages for all trajectories) because then the required computer time is proportional to N_T rather than N_T^2. This situation occurs for example for the rigid-rod model with the constant diffusion coefficient and the Maier–Saupe potential investigated in detail by Marrucci and Maffettone;[8] for that model, ensembles of several hundred thousands of trajectories can be simulated easily.

For all simulations it is important to obtain results not only for large values of N_T but also for small Δt, because we are interested in the continuous time model as defined in eq 1. For a large value of N_T and a small value of Δt, one obtains a nearly rigorous simulation result for the exact model subject only to statistical errors, and these can be estimated from the fluctuations in the simulation results. Here, we used $N_T = 10\,000$ and $\Delta t = 0.005$, with the time t made dimensionless using the isotropic rotary diffusivity D_r.

References and Notes

(1) Srinivasarao, M.; Berry, G. C. *J. Rheol.* **1991**, *35*, 379.
(2) Burghardt, W. R.; Fuller, G. G. *Macromolecules* **1991**, *24*, 2546.
(3) Pieranski, P.; Guyon, E. *Phys. Rev. Lett.* **1974**, *32*, 924; *Commun. Phys.* **1976**, *1*, 45.
(4) Cladis, P. E.; Torza, S. *Phys. Rev. Lett.* **1975**, *35*, 1283.
(5) Semenov, A. N. *Zh. Eksp. Teor. Fiz.* **1983**, *85*, 549.
(6) Kuzuu, N.; Doi, M. *J. Phys. Soc., Jpn.* **1983**, *52*, 3486; **1984**, *53*, 1031.
(7) Doi, M. *Ferroelectrics* **1980**, *30*, 247. Doi, M.; Edwards, S. F. *The Theory of Polymer Dynamics*; Oxford Press: London, 1986.
(8) Marrucci, G.; Maffettone, P. L. *Macromolecules* **1989**, *22*, 4076; *J. Rheol.* **1990**, *34*, 1217; erratum **1991**, *35*, 313.
(9) Larson, R. G. *Macromolecules* **1990**, *23*, 3983.
(10) Kiss, G.; Porter, R. S. *J. Polym. Sci., Polym. Symp.* **1978**, *65*, 193.
(11) Kiss, G.; Porter, R. S. *J. Polym. Sci., Polym. Phys. Ed.* **1980**, *18*, 361.
(12) Navard, P. *J. Polym. Sci., Polym. Phys. Ed.* **1986**, *24*, 435.
(13) Gotsis, A. D.; Baird, D. G. *Rheol. Acta* **1986**, *25*, 275.
(14) Prasadarao, M.; Pearce, E. M.; Han, C. D. *J. Appl. Polym. Sci.* **1982**, *27*, 1343.
(15) Magda, J. J.; Baek, S.-G.; de Vries, L.; Larson, R. G. *Macromolecules* **1991**, *24*, 4460.
(16) Paper 12: Aldermann, N. J.; Mackley, M. R. *Faraday Discuss. Chem. Soc.* **1985**, *79*.
(17) Gleeson, J.; Larson, R. G.; Mead, D. W.; Kiss, G.; Cladis, P. *Liq. Cryst.*, in press.
(18) Zuniga, I.; Leslie, F. M. *Liq. Cryst.* **1989**, *5*, 725.
(19) Carlsson, T. *Mol. Cryst. Liq. Cryst.* **1984**, *104*, 307.
(20) Burghardt, W. R.; Fuller, G. G. *J. Rheol.* **1990**, *34*, 959.
(21) Onsager, L. *Ann. N.Y. Acad. Sci.* **1949**, *51*, 627.
(22) Larson, R. G. *Recent Developments in Structured Continua*; Longman: London, 1990; Vol. 2.
(23) Hinch, E. J.; Leal, L. G. *J. Fluid Mech.* **1973**, *57*, 753.
(24) Dubois-Violett, E.; Durand, G.; Guyon, E.; Manneville, P.; Pieranski, P. *Solid State Phys.* **1978**, Suppl. 14, 147.
(25) Manneville, P.; Dubois-Violett, E. *J. Phys. (Paris)* **1976**, *37*, 285.
(26) Berry, G.; Srinivasarao, M. *J. Stat. Phys.*, in press.
(27) Bruinsma, R.; Safinya, C. R. *Phys. Rev. A* **1991**, *43*, 5377.
(28) Ernst, B.; Navard, P. *Macromolecules* **1989**, *22*, 1419.
(29) Takebe, T.; Hashimoto, T.; Ernst, B.; Navard, P.; Stein, R. *J. Chem. Phys.* **1990**, *92*, 1386.
(30) Viola, G. G.; Baird, D. G. *J. Rheol.* **1986**, *30*, 601.
(31) Picken, S. J.; Aerts, J.; Doppert, H. L.; Reuvers, J.; Northolt, M. G. *Macromolecules* **1991**, *24*, 1366.
(32) Kiss, G.; Porter, R. S. *Mol. Cryst. Liq. Cryst.* **1980**, *60*, 267.
(33) Doi, M.; Edwards, S. F. *J. Chem. Soc., Faraday Trans. 2* **1978**, *74*, 918.
(34) Messiah, A. *Quantum Mechanics*; North-Holland: Amsterdam, The Netherlands, 1972, Vols. 1 and 2.
(35) Gardiner, C. W. *Handbook of Stochastic Methods for Physics, Chemistry and the Natural Sciences*; Springer: Berlin, 1983.
(36) Honerkamp, J.; Seitz, R. *J. Chem. Phys.* **1987**, *87*, 3120.